Earth Planet. Sci. Lett. 684 (2026) 119961

Contents lists available at ScienceDirect

Earth and Planetary Science Letters

journal homepage: www.elsevier.com/locate/epsl

Paleodirections and paleointensity of the Zimbros dikes (South Brazil): Evidence for ultralow fields and hints of a dipole in the mid-Ediacaran

Camila R. Tomé [a,*], Jairo F. Savian [a,b], Wellington P. de Oliveira [c], Gelvam A. Hartmann [c], João A.S. Fontoura [a], Mathew Domeier [d], Filipe A. Temporim [e], Ruth Hinrichs [a], Ricardo I.F. Trindade [f], Maria de Fátima Bitencourt [a,b]

[a] Programa de Pós-graduação em Geociências, Universidade Federal do Rio Grande do Sul, Av. Bento Gonçalves, 91540-000, Porto Alegre, Brazil
[b] Instituto de Geociências, Universidade Federal do Rio Grande do Sul, Av. Bento Gonçalves, 9500, 91540-000, Porto Alegre, Brazil
[c] Instituto de Geociências, Universidade Estadual de Campinas, Rua Carlos Gomes 250, 13083-855, Campinas, Brazil
[d] Centre for Planetary Habitability, University of Oslo, Norway
[e] Departamento de Geologia, Universidade Federal de Ouro Preto, Rua Nove, 35402-163, Ouro Preto, Brazil
[f] Departamento de Geofísica, Instituto de Astronomia, Geofísica e Ciências Atmosféricas, Universidade de São Paulo, Rua do Matão, 1226, 05508-090, São Paulo, Brazil

ARTICLE INFO

Editor: Dr C Carolina Lithgow-Bertelloni

Keywords:
Paleomagnetism
Paleointensity
Ediacaran
Zimbros intrusive suite
South Brazil

ABSTRACT

Ediacaran (635–538 Ma) paleomagnetic records from multiple continents are associated with populations of paleopoles nearly synchronous in time but widely separated in space. Some hypotheses to explain these data appeal to rapid motions of the solid Earth, whereas others invoke a non-geocentric axial dipole (GAD) or an extremely weak GAD field with high paleosecular variation and frequent reversals. We present new directional and absolute paleointensity constraints obtained from two mafic dikes of the Zimbros Intrusive Suite (ca. 590 Ma) in the Dom Feliciano Belt (DFB), southern Brazil. Magnetite and low-Ti titanomagnetite are the main magnetic carriers, associated with pseudo-single-domain to multidomain magnetic behavior. Directional analyses reveal that the dikes host two distinct magnetization components. The low-temperature component is attributed to pyrrhotite, likely related to late-stage tectonic events. The high-temperature component, held by low-Ti titanomagnetite/magnetite, is interpreted as the characteristic remanent magnetization. This component's directions are antipodal and compatible with a dominantly GAD field, but a high degree of directional dispersion may reflect an unstable field. Absolute paleointensity experiments yielded 19 reliable estimates with virtual dipole moments (VDM) of $0.38 \pm 0.15 \times 10^{22}$ and $0.89 \pm 0.33 \times 10^{22}$ Am^2. The validity of these ultra-low estimates was confirmed by their stability under progressively stricter selection criteria based on curvature analysis, indicating the estimates' internal consistency. The obtained VDMs are consistent with coeval results from Laurentia and Baltica, and with an existing time-averaged field estimate from the DFB. Together, these results provide additional evidence of a remarkably weak Ediacaran geomagnetic field.

1. Introduction

The Ediacaran Period (ca. 635–538 Ma) was a time of profound transformation in Earth's history, marked by significant changes in the biosphere, biogeochemical cycles, oceans, atmosphere, climate, and global tectonic activity. Major events included the appearance and diversification of macroscopic metazoan life, large-scale glaciations, extreme carbon isotope excursions, and potentially a rise in atmospheric oxygen (e.g., Och and Shields, 2012; Meert et al., 2016; Xiao and Narbonne, 2020). Important changes also occurred in global paleogeography, including the terminal breakup of the supercontinent Rodinia and the assembly of Gondwana (e.g., Li et al., 2013; Robert et al., 2021). In addition, this period has been associated with significant changes in the behavior of the geomagnetic field (Abrajevitch and Van der Voo, 2010; Halls et al., 2015; Bono et al., 2019; Domeier et al., 2023).

The Ediacaran paleomagnetic record is notably complex. Apparent polar wander paths (APWPs) from several continents, including Laurentia, Baltica, and West Africa, display abrupt directional shifts, and the

* Corresponding author at: Centro de Estudos de Geologia Costeira e Oceânica, Universidade Federal do Rio Grande do Sul, Av. Bento Gonçalves, 9500, 91540-000, Porto Alegre, Brazil.
E-mail address: camilarocha.tome@gmail.com (C.R. Tomé).

https://doi.org/10.1016/j.epsl.2026.119961
Received 19 July 2025; Received in revised form 23 February 2026; Accepted 2 March 2026
Available online 8 April 2026

underlying paleopoles appear to cluster into two or more spatially distinct, yet nearly coeval, populations (e.g., Domeier et al., 2023). Interpreted under the assumption of a geocentric axial dipole (GAD) field, these data would seem to require extremely fast drift rates of the tectonic plates (e.g., Meert et al., 1993; Zahirovic et al., 2015) and/or the occurrence of very rapid true polar wander (e.g., Wen et al., 2022). However, the motion rates implied by these data appear to exceed those considered geodynamically plausible for either differential plate motion or true polar wander (e.g., Cottrell et al., 2023; Domeier et al., 2023; Robert et al., 2023).

As an alternative to fast motions of the solid Earth, the unusual Ediacaran paleomagnetic data could instead reflect a non-GAD field structure (e.g., Abrajevitch and Van der Voo, 2010; Robert et al., 2023) or a very weak GAD field (Bono et al., 2019; Shcherbakova et al., 2020; Thallner et al., 2021a;2021b; Thallner et al., 2022; Huang et al., 2024), characterized by frequent geomagnetic reversals (e.g., Halls et al., 2015; Bazhenov et al., 2016; Meert et al., 2016; Levashova et al., 2021) or a very high paleosecular variation (e.g., Bono and Tarduno, 2015). In a non-GAD scenario, the geomagnetic field would be dominated by higher-order components, such as quadrupoles or octupoles, or a non-axial dipole, such as an equatorial dipole (Abrajevitch and Van der Voo, 2010), whose spatial fixation would require persistent thermal heterogeneities at the core-mantle boundary. Another possibility is that the apparently discrepant paleomagnetic results are due to unrecognized data artifacts (Bono and Tarduno, 2015).

Paleointensity data offer an independent constraint on geomagnetic field behavior, and existing Ediacaran paleointensity estimates are exceptionally low (Bono et al., 2019; Shcherbakova et al., 2020; Thallner et al., 2021a, 2021b; Thallner et al., 2022). Geodynamo models indicate that the geomagnetic field may have operated in a weakened regime during the Neoproterozoic, in response to a decrease in convective power preceding inner core nucleation (ICN - Driscoll, 2016), and ultra-low Ediacaran paleointensities have been interpreted to possibly mark the time immediately prior to ICN onset (e.g., Zhou et al., 2022, 2024). Subsequent ICN may have led to a rapid strengthening of the dipolar field driven by the introduction of new sources of thermal and compositional buoyancy (e.g., Driscoll, 2016; Zhou et al., 2022), and some early Cambrian paleointensity data (ca. 532 Ma) have suggested that the field strength increased substantially then, supporting ICN at around 550 Ma (Zhou et al., 2022).

Despite their importance, paleointensity data from the Ediacaran and early Cambrian remain sparse. This is in part because absolute paleointensity studies are demanding in terms of the magnetic carriers required: preferably non-interacting, single-domain (SD) grains that preserve a primary thermoremanent magnetization, and comprising a population that averages paleosecular variation (e.g., Néel, 1949; Dunlop, 2011; Tarduno et al., 2025). However, Ediacaran rocks have often undergone complex geologic histories and/or host non-ideal carriers, resulting in low experimental success rates. Furthermore, the global PINT database, which compiles absolute paleointensity records over the last 4 billion years, exhibits a pronounced spatial bias, with nearly 90% of the data originating from the Northern Hemisphere (Bono et al., 2022b). For the Ediacaran, published paleointensity estimates come exclusively from Laurentia and Baltica (Bono et al., 2019; Shcherbakova et al., 2020; Thallner et al., 2021a, 2021b; Thallner et al., 2022), except for one recent constraint from the Dom Feliciano Belt of southern Brazil (Huang et al., 2024). Additional Ediacaran paleointensity constraints—particularly from the Southern Hemisphere—are therefore essential to better constrain the evolution of the geomagnetic field through this critical interval.

In this paper, we present new directional and absolute paleointensity data from two mafic dikes of the Zimbros Intrusive Suite (ca. 590 Ma), located in the northern segment of the Dom Feliciano Belt (DFB), southern Brazil. The DFB represents the southern portion of the Mantiqueira Province, formed during the collision of the Rio de la Plata, Congo, and Kalahari cratons. Although the data are limited to two dikes and therefore represent essentially instantaneous records of the geomagnetic field, they provide further evidence of a globally weakened geomagnetic field regime during the Ediacaran.

2. Geological setting

The Dom Feliciano Belt corresponds to the southern segment of the Neoproterozoic orogenic system known as the Mantiqueira Province, resulting from the amalgamation of the Rio de la Plata, Congo, and Kalahari cratons (Fig. 1a). The DFB is divided into Southern, Central, and Northern sectors and comprises most of the shield areas in Uruguay and in the Brazilian states of Rio Grande do Sul and Santa Catarina, respectively (Fig. 1b). The Eastern part of the Central and Northern sectors features an Ediacaran post-collisional batholith (De Toni et al., 2024) associated with the development of the Southern Brazilian Shear Belt (SBSB), a lithospheric-scale structure composed of multiple shear zones that promoted the activation of mantle sources previously modified by subduction, and crustal melting processes (Bitencourt and Nardi, 2000). In Santa Catarina, post-collisional magmatism (ca. 650–540 Ma) is represented by the Florianópolis Batholith, a multi-stage igneous body that is partly emplaced within the Major Gercino Shear Zone (MGSZ), a large structure that cuts across the batholith's northern portion (Fig. 1c; Bitencourt et al., 1989a; Bitencourt, 1996). The MGSZ is a NE-striking, dextral transcurrent shear zone with a subordinate oblique component (Bitencourt et al., 1989a; Bitencourt, 1996).

The Porto Belo-Bombinhas region is almost entirely located in the MGSZ (Fig. 1d), except for its southeastern portion, where the structures related to the shear zone are poorly developed. The basement rocks in this area consist of an association of orthogneisses and granitoids, with U-Pb zircon ages ranging from 798 $\pm$ 3.8 Ma to 609 $\pm$ 8.3 Ma (Chemale Jr. et al., 2012; De Toni et al., 2020; Peruchi et al., 2021). The Zimbros Intrusive Suite (ZIS) (Fig. 1d) comprises late-stage magmatic events relative to the MGSZ activity, and U-Pb zircon ages from several ZIS components are reported by Chemale Jr. et al. (2012). These include the Zimbros (LA-ICP-MS, 587 $\pm$ 8 Ma) and Morro dos Macacos (U-Pb TIMS, 588 $\pm$ 3 Ma) granites, the former found within the shear zone and the latter nearby, but outside the main structure, thus recording only minor deformation features. The hypabyssal part of the suite (zircon SHRIMP, 587 $\pm$ 9 Ma) is a swarm of vertical to subvertical dikes emplaced parallel to the shear zone, where felsic dikes predominate over mafic ones, and occasionally form composite dikes, with mafic margins and felsic cores (Bitencourt, 1996). The dike swarm is located in a ~1 km-wide strip southeast of the Zimbros Granite, with only a few intrusions outside the main zone (Fig. 1d). Structural and magnetic fabric data indicate that the emplacement of these rocks was syntectonic, with predominantly subhorizontal magma flow parallel to the regional stretching direction of the MGSZ (Tomé et al., 2020). However, the main zone of dike emplacement corresponds to a low-strain area, where the MGSZ mylonitic foliation is weakly developed or absent. The felsic hypabyssal rocks are porphyritic rhyolites and dacites, while the mafic ones consist mainly of diabase.

3. Materials and methods

3.1. Sampling

Paleomagnetic sampling was conducted on mafic and felsic dikes from the Zimbros Bay region during three field seasons. A total of five mafic dikes (CT-33, CT-34, CT-35, CT-38, and CT-47) and one felsic dike (CT-16) were sampled. The mafic dikes corresponding to sites CT-35 and CT-38, which yielded the paleointensity results, strike NE-SW (040°-060°) and dip steeply (70°-90°) to the SE or NW (Supplementary Fig. 1). The CT-35 dike is approximately 2 m thick and can be traced for about 150 m, whereas the CT-38 dike is about 1.4 m thick and extends for roughly 80 m. Both exhibit sharp contacts with the host rocks. At each site, at least six cores measuring approximately 8 cm in length and 2.5

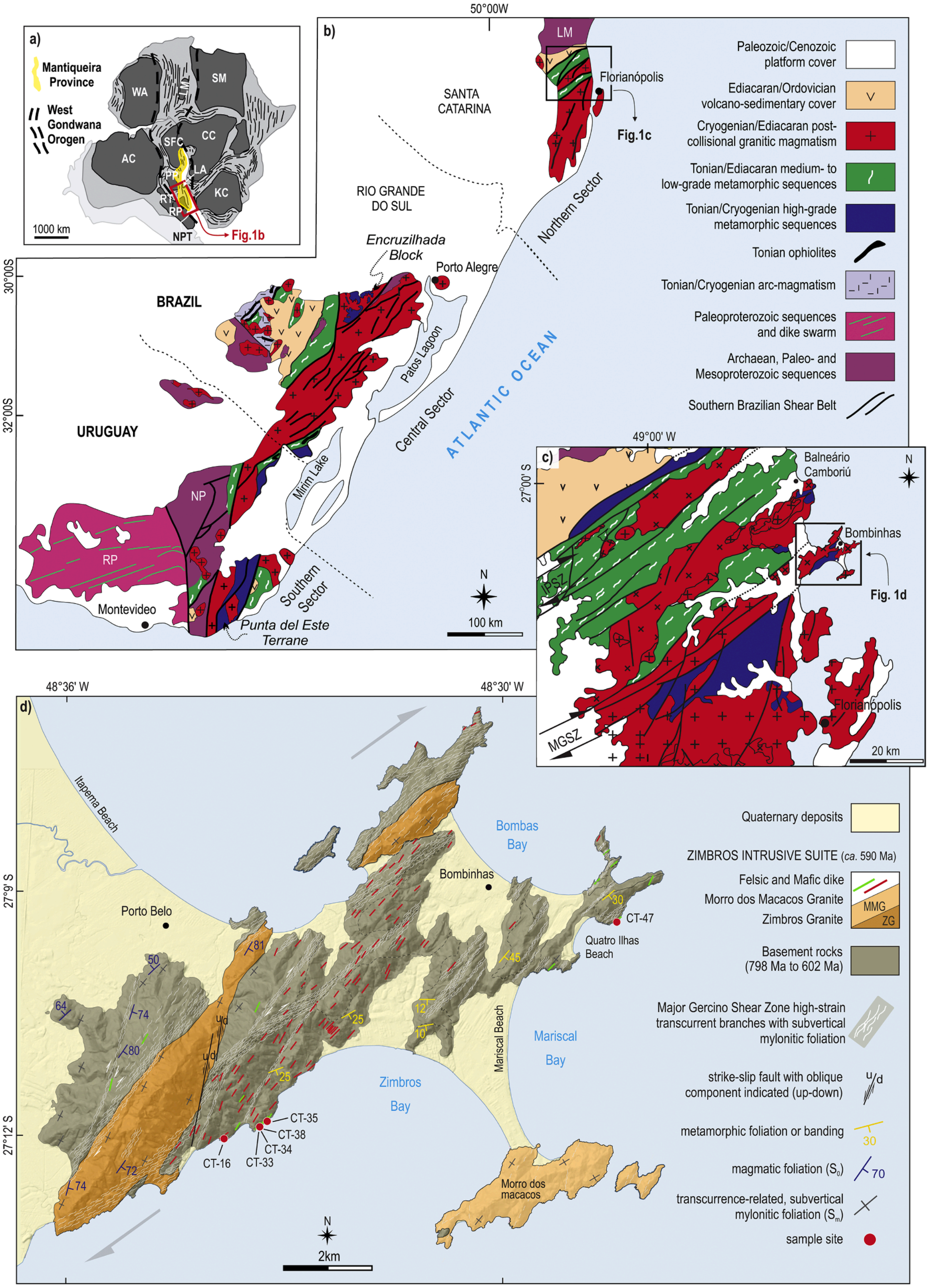

Fig. 1. a) Geotectonic sketch of Western Gondwana showing its main crustal blocks and orogenic belts (modified from Oriolo et al., 2017): WAC-West Africa Craton; LM-LATEA Metacraton; SM-Sahara Metacraton; AC-Amazonian Craton; SFC-São Francisco Craton; CC-Congo Craton; KC Kalahari Craton; RPC- Rio de La Plata Craton; PP-Paranapanema Plate; LA-Luis Alves Microplate; NPT-Nico Pérez Terrane. b) Geotectonic framework of the Dom Feliciano Belt and surrounding cratonic areas (modified from Bitencourt and Nardi, 2000). c) Inset showing the geological units and tectonic domains of Santa Catarina State, with indication of the study area (modified from De Toni et al., 2024). MGSZ Major Gercino Shear Zone; IPSZ-Itajaí-Perimbó Shear Zone. d) Geological map of the Porto Belo and Bombinhas region, showing the sampling sites, with emphasis on the granites and subvolcanic rocks of the Zimbros Intrusive Suite. The undifferentiated host rocks include orthogneisses and granitoids (modified from Bitencourt, 1996).

cm in diameter were extracted using an adapted portable gasoline-powered drill. The orientation of each core was determined using both magnetic and sun compasses. The geographic coordinates of the sampling sites were recorded using a handheld GPS device. In total, 62 oriented cores were collected. In the laboratory, these cores were cut into standard cylindrical specimens measuring 2.2 × 2.5 cm (length x diameter), yielding 170 specimens. For absolute paleointensity experiments, a subset of the specimens was drilled to produce smaller sub-specimens measuring approximately 1 × 1 cm (length x diameter), resulting in 96 sub-specimens suitable for the paleointensity experiments.

3.2. Methods

Characterization of the magnetic carriers and evaluation of their stability were conducted through a series of rock magnetic experiments, including low-field magnetic susceptibility versus temperature (K-T) measurements, hysteresis parameter analysis, isothermal remanent magnetization (IRM) acquisition curves, and first-order reversal curves (FORCs). These analyses were performed on samples from six dikes selected for paleomagnetic and paleointensity studies. All experiments were carried out at Laboratório de Paleomagnetismo e Magnetismo de Rochas, Universidade de São Paulo (USPMag), Brazil.

3.2.1. Rock magnetism

To identify the magnetic carriers, low-field magnetic susceptibility measurements as a function of temperature (K-T) were performed from room temperature to 700 °C in an argon atmosphere to avoid oxidation. The measurements were made with an AGICO Kappabridge KLY-4S with a CS4 furnace. Curie temperatures were determined from the derivative of the K(T) heating curves using the finite difference method (dK/dT).

Hysteresis loops, IRM acquisition curves, and FORC diagrams were measured at room temperature with a MicroMag 3900 vibrating sample magnetometer, using applied fields of up to 1T. Coercive force (Hc), saturation magnetization (Ms), and saturation remanent magnetization (Mrs) were estimated after subtraction of the paramagnetic contribution from the high field portion of hysteresis curves. The coercivity of remanence (Hcr) was determined from backfield measurements following sample saturation in a field of 1 T. IRM acquisition curves were obtained using a non-linear sequence of 150 measurement points and a maximum field of 1 T. IRM acquisition curves were submitted to unmixing analysis using MAX UnMix software (Maxbauer et al., 2016). FORC diagrams (Roberts et al., 2000) were generated from 300 reversal curves measured at room temperature, using a range of -150 to 150 for Bu and 0 to 150 mT for Bc, and an averaging time of 300 ms. The data were processed using the FORCinel software package (Harrison and Feinberg, 2008) with a smoothing factor of 4 for all samples.

To further characterize the magnetic oxides, Scanning Electron Microscopy (SEM) was performed on three polished sections using a JEOL JSM-5800 SEM instrument. Samples were examined with a Thermo Fisher Scientific Si(Li) EDX detector, operated through the Noran System Six software. Spectra and images were acquired at an accelerating voltage of 15 kV. Backscattered electron images (BEIs) were processed in image analysis software (ImageJ, National Institutes of Health). All analyses were conducted at Laboratório de Microanálise do Instituto de Física da Universidade Federal do Rio Grande do Sul (UFRGS), Brazil.

3.2.2. Paleomagnetic data

Paleodirectional experiments were conducted using alternating-field demagnetization (AFD) and thermal demagnetization (THD) to identify the magnetization components in the samples. A total of 170 specimens were measured in this study. Natural remanent magnetization (NRM) measurements were carried out using an AGICO JR6A spinner magnetometer with a sensitivity of 2.4×10^{-6} A/m. For thermal demagnetization, two protocols were employed: one corresponding to the same protocol used in the paleointensity experiments (see below) and the other following specific temperature increments, consisting of steps of 50 °C (100–500 °C), 20 °C (500–560 °C), 10 °C (560–580 °C), and 20 °C (580–680 °C). The procedure was performed in a thermal demagnetization oven (model TD48 SC; ASC Scientific). AFD was conducted using an AGICO LDA5 demagnetizer, with steps of 1 mT (1–10 mT), 2 mT (10–20 mT), 5 mT (20–50 mT), and 10 mT (50–100 mT). Combined AFD-THD was also performed on two specimens from each site to test the stability of the magnetization after the removal of low-coercivity components associated with the presence of multidomain (MD) titanomagnetite or magnetite grains. For this purpose, the protocol consisted of two AFD steps at 5 and 10 mT, followed by THD steps using the THD protocol described above. All analyses were performed in a magnetically shielded room with an ambient field below 500 nT. Magnetic components were identified through principal component analysis (PCA) (Kirschvink, 1980), and the site-mean directions were calculated using Fisher statistics (Fisher, 1953). All mean directions are reported in situ.

3.2.3. Paleointensity

Paleointensity experiments were performed on 96 specimens of 1 cm^3 using the double-heating Thellier method (Thellier and Thellier, 1959) modified by Coe (1967), in which zero-field steps are followed by in-field steps (the so-called TT-ZI protocol). Our TT-ZI protocol consisted of 54 heating-cooling steps from room temperature (~20 °C) to 600 °C, with verification steps (pTRM checks and pTRM tail checks) included throughout the heating sequence. The specimens were progressively heated with temperature increments of 50 °C from 100 °C to 300 °C, 25 °C intervals between 300° and 400 °C, and then 20 °C intervals up to 600 °C. Partial thermoremanent magnetization (pTRM) checks were conducted at selected temperature steps (150 °C to 560 °C), approximately every 50 °C, to continuously monitor TRM stability. Additionally, pTRM tail checks were performed at five temperature steps (200 °C, 300 °C, 400 °C, 500 °C, and 600 °C) to assess potential multidomain behavior. The procedure included an additional zero-field step following each double-heating ZI step. This allows the identification of pTRM 'tails,' which correspond to the fraction of magnetization acquired at a given blocking temperature that is not completely erased after subsequent zero-field heating at the same temperature. The presence of significant tails indicates MD behavior, in which the blocking and unblocking temperatures do not coincide. The heating and cooling cycles were strictly controlled to 30 min each, and the position of the specimens within the oven was kept constant throughout the experiment. A laboratory field of 10 μT was applied parallel to the specimen's x-axis during the thermal treatments. Magnetization measurements were performed using a horizontal SQUID magnetometer (Superconducting Quantum Interference Device, 2 G Enterprises), installed in a magnetically shielded room.

Selection criteria for the paleointensity data were established based on the Standard Paleointensity Definition (SPD; Paterson et al., 2014) and on criteria applied in paleointensity studies of Ediacaran rocks (e.g., Thallner et al., 2021a, 2021b, 2022; Huang et al., 2024). Specimens were classified into two quality categories (A and B) based on these paleointensity statistical parameters. For category A, at least four points ($n \geq 4$) were required for the best-fit line on the Arai plot (Nagata, 1963). The dispersion parameter around the best-fit line (β) was required to be ≤ 0.15. The linearity of the selected segment was evaluated using the curvature parameter (Paterson, 2011), adopting a threshold of $|k'| \leq 0.48$. The paleointensity quality factor (q) was required to be ≥ 2. In addition, at least three temperature steps were required for the pTRM checks, with variations within 15 %. The maximum deviation of a pTRM check normalized by the best-fit segment length (DRAT) was required to be ≤ 0.15. The cumulative DRAT (CDRAT), calculated as the sum of all pTRM checks, was also required to be ≤ 0.15. The pTRM tail check deviation (DRATTail) was required to be ≤ 0.15, and the maximum absolute difference of the pTRM check (δt*) was required to be ≤ 0.10. The maximum angular deviation (MAD) of the characteristic remanent magnetization (ChRM) direction had to be ≤ 15°. Category B includes specimens that failed to meet one of the criteria required for category A. Specimens with significantly discrepant ancient field intensity (Banc) values were considered anomalous and excluded from the final mean calculation, unless other selection parameters were within acceptable limits, in which case they were assigned to category B. Data analysis was carried out using the Pmag GUI software (Tauxe et al., 2016) and the paleointensity.org platform (Béguin et al., 2020).

4. Results

4.1. Magnetic mineralogy

The high-temperature thermomagnetic curves of samples CT-35F and CT-38G, both from mafic dikes, exhibit similar behavior, with abrupt drops in susceptibility between approximately 572 °C and 577 °C (Fig. 2a-b). The numerical derivatives of these curves (dK/dT) indicate the presence of magnetite and/or low-Ti titanomagnetite. The hysteresis loops, corrected to remove diamagnetic and paramagnetic contributions (Fig. 2c-d), show narrow shapes, with low remanence values (Mrs/Ms around 0.05–0.06) and coercivity ratios (Hcr/Hc) of 3.85 (sample CT-

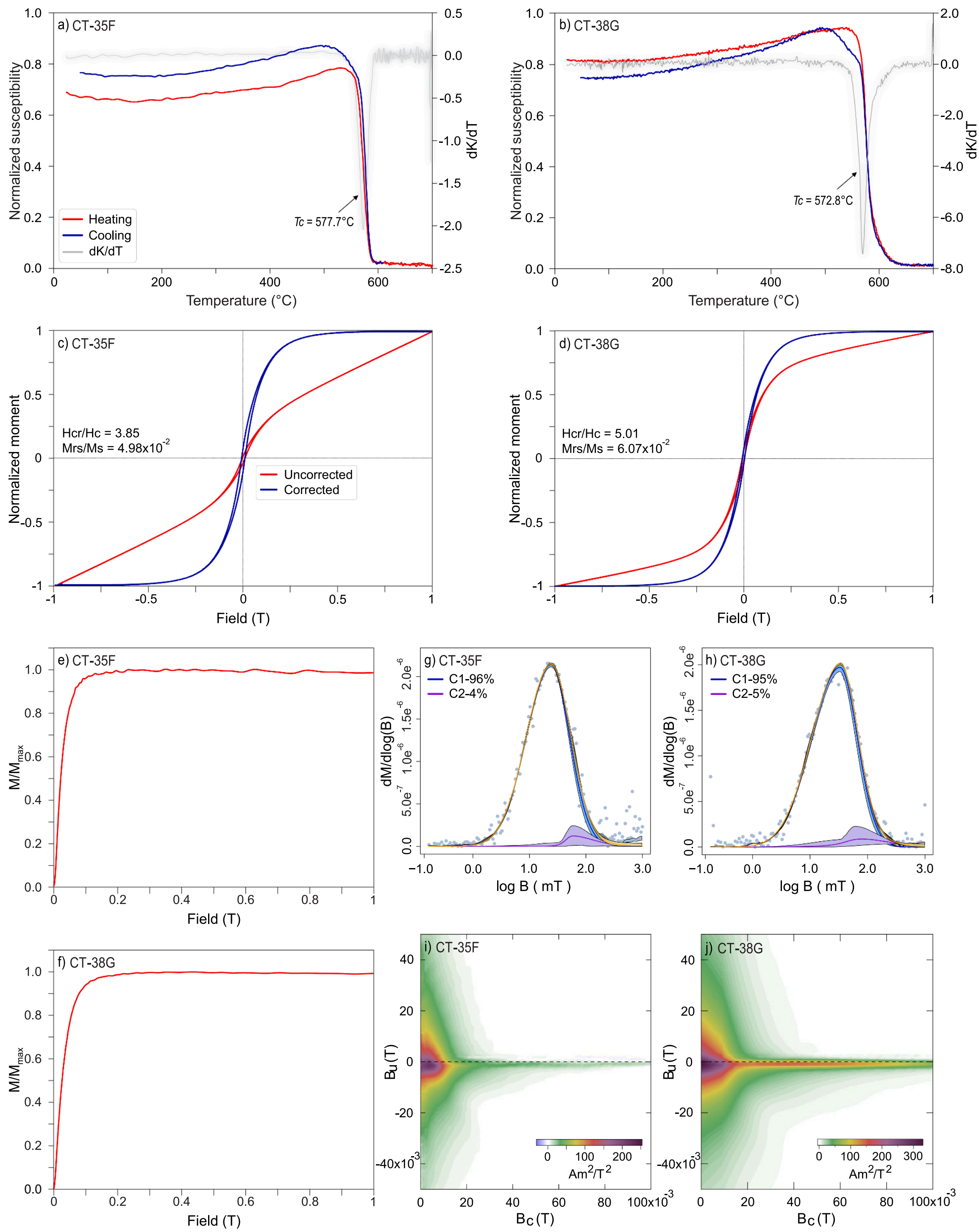

Fig. 2. Magnetic mineralogy dataset for samples CT-35F and CT-38G. a-b) Normalized magnetic susceptibility curves as a function of temperature during heating (red line) and cooling (blue line) cycles, with numerical derivative (dK/dT, gray line) indicating Curie temperatures (Tc). c-d) Normalized hysteresis loops showing coercivity (Hcr/Hc) and remanence (Mrs/Ms) ratios typical of multidomain (MD) to pseudo-single-domain (PSD) grains. Red lines are uncorrected; blue lines are corrected to remove diamagnetic and paramagnetic contributions. e-f) IRM acquisition curves reaching saturation in fields below 0.3 T. g-h) Magnetic component coercivity spectra obtained by MAX UnMix modeling (Maxbauer et al., 2016). i-j) FORC diagrams showing broad distributions centered along the coercivity axis (Bc), with low spread along the interaction axis (Bu), indicative of MD to PSD grains with weak magnetic interactions.

35F) and 5.01 (CT-38G). These parameters indicate low-coercivity minerals compatible with magnetite in pseudo-single-domain (PSD) or vortex states, and in MD states (e.g., Day et al., 1977; Dunlop and Özdemir, 1997; Dunlop, 2002; Roberts et al., 2019). The IRM acquisition curves (Fig. 2e-f) indicate full saturation under fields below 0.3 T, reinforcing the dominance of low-coercivity minerals. The coercivity distribution modeling using MAX UnMix (Fig. 2g-h) shows that both samples are dominated by a low-coercivity population (C1: 95–96 %), with coercivity peaks (Bh) around 0.02 T and dispersions (DP) ranging from 0.38 to 0.40 log units. These values are consistent with PSD-MD magnetite (e.g., Dunlop and Özdemir, 1997). Additionally, a secondary fraction (C2: 4–5 %) is identified, with Bh peaks of approximately 0.12 T and DP values from 0.36 to 0.47 log units, suggesting the presence of a high-coercivity population, possibly associated with iron sulfides such as pyrrhotite (e.g., Rochette et al., 1990; Dunlop and Özdemir, 1997). The FORC diagrams (Fig. 2i-j; Supplementary Fig. 3) reveal evidence of distinct contributions from different magnetic domain-states. Most samples display low coercivity (Bc) and strong vertical spreading along the interaction field axis (Bu), indicating a dominant MD signal (e.g., Roberts et al., 2000). A PSD or vortex-state contribution with slightly higher Bc and a three-lobed pattern is also observed, particularly in CT-34D (Supplementary Fig. 3) and CT-38G (Fig. 2j). Overall, the diagrams indicate a mixture of MD and PSD/vortex signals (e.g., Roberts et al., 2000; 2019). Sample CT-38G, however, displays a subordinate SD signal, with higher Bc and a narrow Bu ridge, reflecting isolated, non-interacting grains. Although pyrrhotite is present in the sample, as evidenced by SEM observations and demagnetization results, it is not detected in the hysteresis or K-T curves. This apparent absence likely reflects the magnetic dominance of magnetite, whose significantly higher susceptibility and saturation magnetization mask the contribution of weaker magnetic phases. Thus, the lack of a diagnostic signature in these data does not necessarily imply the absence of the mineral, but rather indicates that the specific SD signal observed in the FORC diagram is not controlled by pyrrhotite. Instead, the SD signal is interpreted as non-interacting magnetite, indicating the presence of ideal carriers capable of retaining a stable ChRM.

Scanning electron microscopy (SEM) analyses (Fig. 3a-d; Supplementary Fig. 4) indicate that titanomagnetite is the main Fe-Ti oxide phase present in the samples, with magnetite occurring subordinately, usually as small euhedral to subhedral crystals (<1–5 μm) or as intergrown lamellae. These opaque phases are disseminated in a matrix rich in mafic minerals, mainly pyroxene and amphibole. In sample CT-35F (Fig. 3a-b), fine crystals of magnetite and titanomagnetite (<5 μm) predominate, along with subhedral titanomagnetite crystals (~30 μm) exhibiting fine, parallel internal lamellae less than 1 μm thick. These textures are typical of exsolution between magnetite and ilmenite, resulting from slow cooling of a homogeneous solid solution (e.g., Haggerty, 1991). In sample CT-38G (Fig. 3c-d), titanomagnetite occurs as subhedral to anhedral crystals, frequently arranged in oriented lamellae. Magnetite is intergrown with titanomagnetite, showing euhedral to elongated morphologies (<20 μm). Iron sulfides such as pyrite and pyrrhotite occur mainly in sample CT-38G, forming euhedral to subhedral crystals. These minerals appear both isolated and associated with Fe-Ti oxides, concentrating in interstices or along oxide margins.

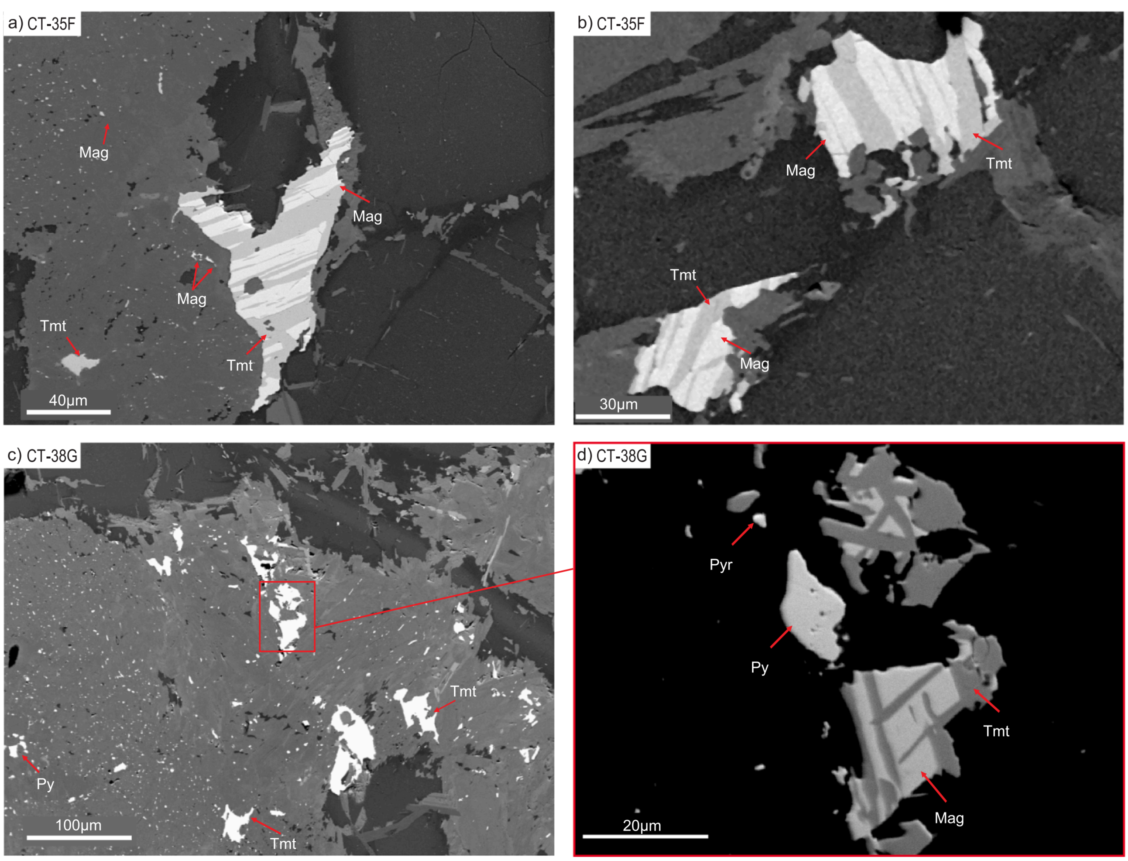

Fig. 3. Backscattered electron (BSE) scanning electron microscopy (SEM) images of Fe-Ti oxides and Fe sulfides in samples CT-35F and CT-38G. a-b) Subhedral titanomagnetite (Tmt) crystals with thin, parallel exsolution lamellae of magnetite (Mag), along with isolated fine-grained magnetite particles (<5 μm), associated with a mafic matrix. c) Overview of sample CT-38G, showing anhedral to subhedral titanomagnetite and Fe sulfide crystals irregularly distributed in a matrix rich in mafic minerals. d) Magnified view of the area highlighted in the image (c), showing intergrowths of titanomagnetite (Tmt), magnetite (Mag), and Fe sulfides, including pyrite (Py) and pyrrhotite (Pyr).

4.2. Paleomagnetic data

Fig. 4 presents examples of alternating field (AFD) and thermal (THD) demagnetization for samples from sites CT-35 and CT-38. In the AFD experiments, samples CT35A1 and CT38C1 exhibited an abrupt drop in NRM during the initial demagnetization steps, corresponding to the removal of a low-coercivity component. With the progressive removal of this low-coercivity component, a second, directionally distinct component becomes discernible and is well isolated upon AFD beyond 50 mT. Although not fully removed, this component displays linear trajectories trending toward the origin in orthogonal vector diagrams and is characterized by an NNE direction with a moderate positive inclination.

Thermal demagnetization results (Figs. 4b, c, e, and f) show consistent behavior across both sites. All samples revealed two distinct components, differentiated by their unblocking temperatures. The first is marked by a sharp drop between 300 °C and 350 °C, consistent with the presence of pyrrhotite (e.g., Dominguez et al., 2011), and is more pronounced in sample CT35B154. Above 350 °C, a second, high-temperature component could be isolated, displaying approximately linear trajectories in vector diagrams. This component persists up to 560–580 °C, suggesting that it is carried by magnetite and/or low-Ti titanomagnetite. At CT-35, the mean direction of this component trends S-SW with moderate to shallow positive inclinations, whereas at CT-38, the direction is NE with moderate to shallow negative inclinations. Comparison between the two methods indicates that at CT-35, the high-coercivity component identified by AFD likely corresponds to the low-unblocking-temperature component observed in the THD treatment. Conversely, at CT-38, the low-coercivity component identified in AFD appears to match the high-temperature component isolated by THD. These results suggest that the same remanent components are recovered by both treatments (and at both sites), and that distinct magnetic phases carry them with contrasting coercive and thermal stabilities.

Site-mean directions were determined by considering at least two specimens from two different cores per site. Of the sampled sites, only CT-35 and CT-38 yielded reliable data for calculating mean directions. Sites CT-16, CT-33, CT-34, and CT-47 were excluded due to directional dispersion or the presence of unstable components (see Supplementary Figs. 2 to 5). Site CT-16, the only felsic dike sampled, exhibited a near-total loss of the NRM at fields below 10 mT and lacked coherent demagnetization trajectories in either treatment. Its magnetic mineralogy also indicates the dominance of MD grains, suggesting possible recent remagnetization (see Supplementary Figs. 2–5). At sites CT-33 and CT-34, the NRM was also nearly completely removed below 10 mT during AFD. Although samples showed linear trajectories in THD,

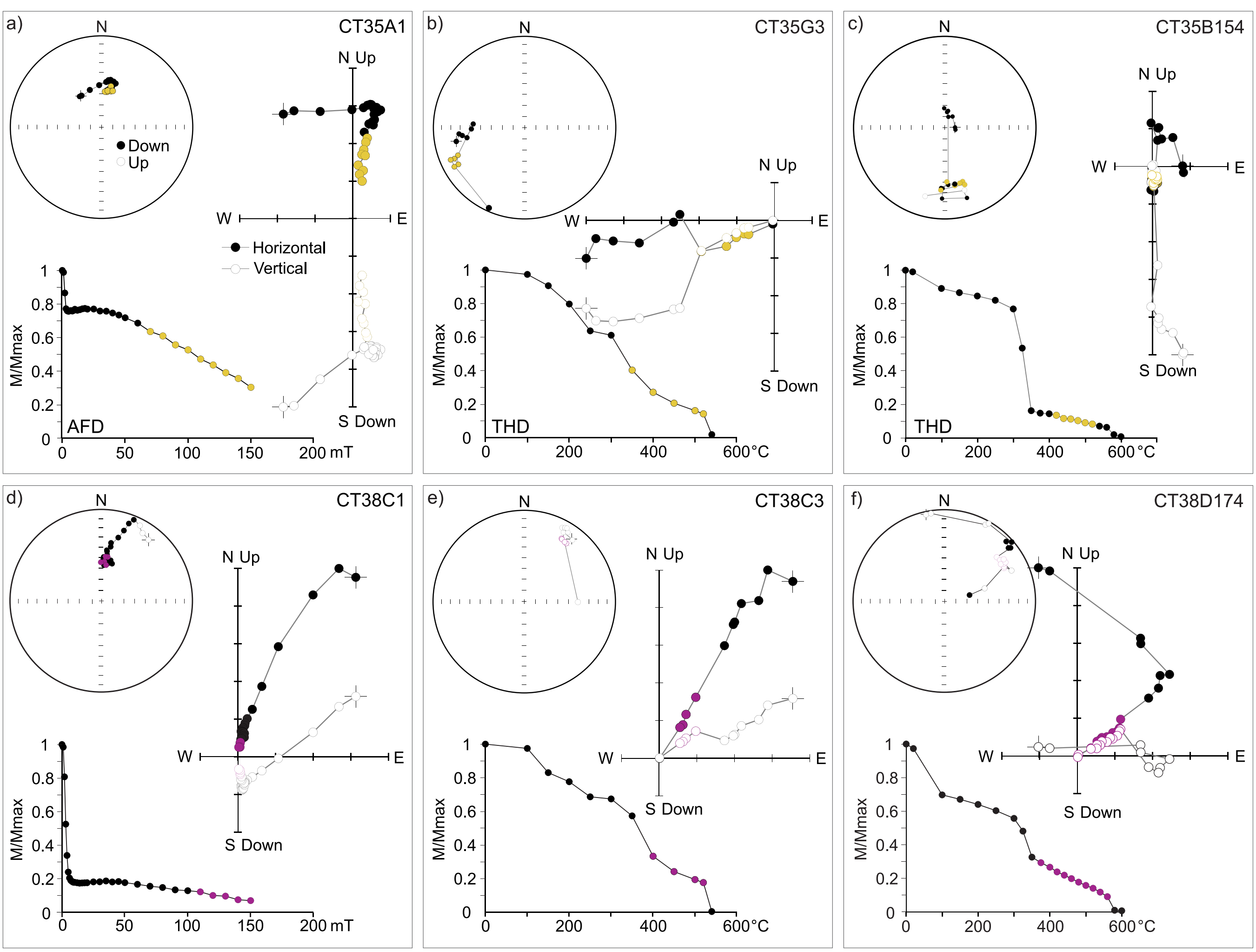

Fig. 4. Representative examples of demagnetization diagrams and orthogonal vector projections (Zijderveld plots) for six selected specimens. Diagrams show alternating field demagnetization (AFD) data for specimens CT35A1 (a) and CT38C1 (d), and thermal demagnetization (THD) data for specimens CT35G3 (b), CT35B154 (c), CT38C3 (e), and CT38D174 (f). AFD and THD plots display normalized magnetization (M/Mmax) as a function of applied field (mT) or temperature (°C), respectively. The characteristic directions determined by principal component analysis (PCA) are highlighted in the orthogonal vector diagrams in yellow (CT-35) and purple (CT-38).

their corresponding directions were widely scattered. Site CT-47, in addition to displaying high directional scatter in both treatments, exhibited complex demagnetization patterns, with evidence of at least three magnetic components in some samples. This behavior is marked by trajectories forming small circles in stereographic projections, indicating the presence of multiple overlapping components (Supplementary Figs. 2–5).

Sites CT-35 and CT-38 exhibit two main directional groupings, referred to here as Component A and Component B (Fig. 5; Table 1). Component A, best defined in the AFD treatment, is characterized by a high coercivity but low thermal stability, internally consistent clustering, and a mean direction trending NNE with steep positive inclinations (CT-35: Dm = 6.0°, Im = 56.2°, k = 160, α_{95} = 3.8; CT-38: Dm = 14.3°, Im = 49.4°, k = 81, α_{95} = 4.5). Component B, which has a lower coercivity but is more thermally stable and better defined in THD, shows distinct features between the sites. At CT-38, the mean direction is NE with moderate to shallow negative inclination (Dm = 34.7°, Im = -24.8°, k = 29, α_{95} = 6.1). At site CT-35, this component is directed toward the S-SW with shallow positive inclinations (Dm = 238.8°, Im = 28.6°, k = 16, α_{95} = 10.0). Site CT-35 shows a lower precision parameter (*k* = 16) than site CT-38 (*k* = 29), indicating slightly greater directional scatter at this site. The larger dispersion in CT-35 results in a broader confidence cone (α95 = 10.0), suggesting a less precise estimate of the mean direction than in CT-38 (α95 = 6.1). This latter direction appears to be approximately antipodal to that recorded at site CT-38, suggesting that the ChRM preserved in these sites records opposite polarities.

4.3. Paleointensity

After applying the paleointensity protocols and selection criteria, a total of 19 reliable paleointensity estimates were obtained from two sites (CT-35 and CT-38), both of which are represented by mafic dikes. As a result, the specimen-level success rate was approximately 20 %, with nine results classified as Category A and ten as Category B (Table 2). Fig. 6a-d presents representative examples of Arai diagrams and orthogonal projections for specimens that met our selection criteria. In all accepted examples, the Arai diagrams display slight curvature (sagging) along their segments, indicating an upward concavity, particularly at intermediate temperature steps (~440–560 °C). This pattern is characteristic of the influence of MD or PSD grains, in which part of the thermoremanent magnetization is acquired and removed non-reciprocally (e.g., Paterson et al., 2015). Analysis of the curvature parameter indicates that a subset of seven specimens yields values within the limit of |k'| ≤ 0.48 (e.g., Paterson et al., 2015), and that six specimens (one from site CT-35 and five from site CT-38; see Table 2) satisfy even more restrictive criteria (|k'| ≤ 0.27; e.g., Paterson, 2011). The accepted specimens display well-defined, nearly linear high-temperature segments (Fig. 6a-d; Supplementary Fig. 6). These intervals were selected for paleointensity calculation, as they exhibit more stable behavior and are less affected by biases associated with the presence of MD grains.

The orthogonal projections reveal the presence of two distinct magnetization components: a low-temperature component, typically removed below 350 °C, and a high-temperature component, isolated between 420 °C and 580–600 °C. Paleointensity values were determined from the temperature interval associated with the ChRM component,

Table 1
Site-mean directions (in geographic coordinates) were obtained for sites CT-35 and CT-38. Directions are organized according to Component A (low thermal stability) and Component B (high thermal stability), as determined from AFD and THD analyses, respectively. N/n indicates the total number of specimens measured and the number of specimens used to calculate the site mean direction. Dec: declination; Inc: inclination; k: precision parameter (concentration); α_{95}: 95 % confidence ellipses.

Site	N/n	Site Coordinates		Site mean direction			
		Lat. (S)	Long. (W)	Dec (°)	Inc (°)	k	α_{95}
Component A							
CT35	39/10	27° 11′ 45.7"	48° 33′ 16.6"	6.0	56.2	160	3.8
CT38	46/14	27° 11′ 47.9"	48° 33′ 20.0"	14.3	49.4	81	4.5
Component B							
CT35	39/15	27° 11′ 45.7"	48° 33′ 16.6"	238.8	28.6	16	10.0
CT38	46/20	27° 11′ 47.9"	48° 33′ 20.0"	34.7	-24.8	29	6.1

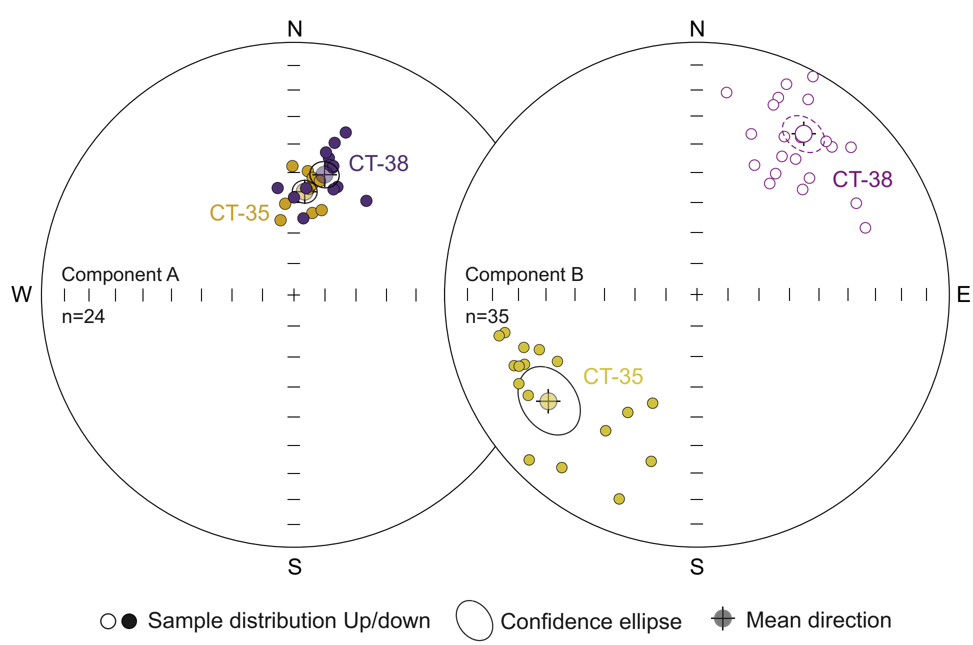

Fig. 5. Stereographic projections show the distribution of mean directions for specimens from sites CT-35 and CT-38. Component A is interpreted as the pyrrhotite-related component, while Component B corresponds to the magnetite and/or low-Ti titanomagnetite component. Open (filled) circles represent upward (downward) directions, respectively. All components are shown in "in situ" coordinates.

Table 2
Paleointensity results from the Zimbros Bay mafic dikes (Hlab = 10 μT). site: name of site sampling; Min temp.-Max temp.: interval temperature used in paleointensity estimates; n: number of points used for the best-fit line on the Arai diagram; Banc: paleointensity estimate; MADanc: Maximum Angular Deviation (anchored fit); DANG: angle between the free-floating best-fit direction and the vector from data center of mass to origin; *f*: NRM fraction used in the fit; β: scatter around the best-fit line (standard error/slope); q: quality factor (combines scatter, NRM fraction, and gap factor); |k'|: curvature parameter of the Arai plot; DRAT: maximum pTRM check deviation normalized by best-fit length; CDRAT: cumulative DRAT; DRAT Tail: maximum pTRM tail check deviation (normalized); δt*: maximum absolute pTRM check difference; Cat: category: reliability classification of the paleointensity result.

Site	Specimen	Min Temp.	Max Temp.	n	B_{anc} (μT)	MAD_{anc}	DANG	*f*	β	q	|k'|	DRAT	CDRAT	DRAT Tail	δt*	Cat.
CT35	CT35A2-49	520	580	4	2.1	7.2	12.4	0.722	0.073	4.5	0.383	6.1	5.8	8.8	0.6	A
	CT35A2-50	520	580	4	2.8	2.7	4.0	0.769	0.149	2.7	0.675	11.1	14.2	9.7	0.4	B
	CT35B1-53	500	580	5	1.8	3.9	1.8	0.733	0.090	5.1	0.455	8.7	1.3	3.0	0.5	A
	CT35B1-54	500	580	5	1.0	12.1	21.4	0.659	0.058	6.4	0.174	8.4	13.4	3.0	0.1	B
	CT35B1-56	520	580	4	2.1	8.1	7.8	0.752	0.076	4.7	0.374	13.1	10.2	5.1	0.1	A
	CT35F1-58	520	600	5	1.0	7.2	9.1	0.825	0.121	3.3	0.915	8.9	7.3	5.7	0.3	B
	CT35F1-60	520	600	5	1.0	9.6	11.3	0.840	0.135	2.5	0.952	10.1	7.5	5.8	2.1	B
	CT35G1-61	520	580	4	1.2	3.4	2.8	0.855	0.095	3.2	0.595	5.0	0.9	4.2	0.2	B
Mean (σ)					***1.63 ± 0.64***											
CT38	CT38A2-66	500	580	5	5.4	5.4	3.6	0.801	0.063	7.2	0.300	14.4	7.1	10.1	0.9	A
	CT38A2-67	500	580	5	4.6	8.8	3.1	0.782	0.064	7.4	0.265	25.9	0.5	9.0	7.5	B
	CT38A2-68	500	600	6	3.1	4.1	3.8	0.778	0.046	10.7	0.247	13.9	4.7	4.6	3.4	A
	CT38B1-71	500	600	6	6.9	4.2	2.1	0.829	0.073	6.6	0.491	14.5	2.0	14.4	1.1	B
	CT38D1-73	500	580	5	3.2	6.0	1.4	0.786	0.085	5.4	0.373	16.1	1.2	4.3	5.6	B
	CT38D1-74	500	600	6	3.1	5.0	2.3	0.809	0.069	7.0	0.493	13.6	5.8	4.2	3.9	B
	CT38F1-75	480	580	6	3.1	4.1	3.7	0.808	0.057	9.6	0.065	5.7	10.0	4.0	3.0	A
	CT38F1-76	500	600	6	4.7	3.8	1.9	0.823	0.083	6.5	0.311	23.3	3.3	11.4	9.3	B
	CT38F1-77	500	600	6	2.1	7.4	5.8	0.757	0.038	12.7	0.135	10.7	11.1	3.2	1.7	A
	CT38F1-78	500	600	6	2.0	3.1	2.3	0.774	0.050	9.5	0.079	14.9	0.7	4.2	3.5	A
	CT38H2-80	500	600	6	3.2	4.3	2.2	0.833	0.054	9.4	0.381	11.9	12.8	5.2	2.7	A
Mean (σ)					***3.78 ± 1.41***											

including only thermal steps with no evidence of magnetic alteration (Fig. 6a-d). In all accepted cases, the high-temperature segments displayed low scatter, good linearity, and positive pTRM checks. The mean intensities obtained were 1.63 ± 0.64 μT for site CT-35 and 3.78 ± 1.41 μT for CT-38 (Table 2). Based on these intensities and the mean inclinations determined from AFD and THD for each site, the calculated VDMs were 0.38 ± 0.15 × 10^{22} Am^2 for site CT-35 and 0.89 ± 0.33 × 10^{22} Am^2 for site CT-38.

Although paleointensity results were satisfactory at sites CT-35 and CT-38, approximately 80 % of the analyzed specimens did not meet the selection criteria. The rejected specimens show pronounced zigzag patterns and upward-concave curvature (sagging) throughout the experiment, indicating TRM instability and possible thermochemical alteration not detected by pTRM checks (Fig. 6e-h; Supplementary Fig. 7; e.g., Shaar and Tauxe, 2015; Tauxe et al., 2021). This non-ideal behavior is reflected in the high failure rates of the |k'| (~78 % of the results), DRAT (~60 %), β (~44 %), and CDRAT (~44 %) quality parameters, indicating that most specimens are dominated by PSD-MD grains, which likely do not preserve a reliable paleointensity record.

To assess the reliability of the site-level paleointensity estimates, we applied the Quality of Paleointensity (QPI) criteria adopted by the PINT database (Bono et al., 2022b). This index comprises 10 quality criteria, originally proposed by Biggin and Paterson (2014) and later refined by Bono et al. (2022a). Among these, the multidomain quality criterion (QMD) is particularly relevant here because it evaluates the extent to which the influence of MD and PSD grains was monitored and controlled during the paleointensity experiments. The Arai diagrams exhibit upward concavity ("sagging"), typical of non-ideal grains, making monitoring this effect especially important. Compliance with the QMD criterion was verified through pTRM-tail checks and by the quantification of the Arai plot curvature (Paterson, 2011). All samples classified as category A met the established selection criteria (Table 2), falling within the curvature limit of $|k'| \leq 0.48$, with a subset satisfying the more restrictive criterion of $|k'| \leq 0.27$. Overall, both sites satisfied four QPI criteria: reliable age (QAGE), indication of primary thermoremanent magnetization (QTRM), control of thermal alteration (QALT), and multidomain bias control (QMD), resulting in a final QPI score of 4 out of 10 for each site.

5. Discussion

The paleodirectional and paleointensity results obtained from two mafic dikes of the Zimbros Intrusive Suite (ca. 590 Ma; sites CT-35 and CT-38) represent instantaneous records of the geomagnetic field. Such records capture the momentary state of the field during the cooling of the rocks and therefore do not provide an estimate of the time-averaged field (TAF) required to assess the long-term behavior of the dynamo (e.g., Tarduno et al., 2025). Despite this inherent limitation of shallow dike emplacement and cooling, our new results provide a valuable contribution to the Ediacaran paleomagnetic database, offering insights into the instantaneous behavior of the geomagnetic field from an observation point beyond Laurentia and Baltica.

The results of our demagnetization and rock magnetic experiments indicate that magnetite and/or low-Ti titanomagnetite are the main carriers of the high-temperature remanence in samples from sites CT-35 and CT-38, and they are mostly associated with PSD to MD behavior. This interpretation is supported by high Curie temperatures, narrow hysteresis loops, and IRM acquisition curves that saturate at low fields (Fig. 2; e.g., Dunlop and Özdemir, 1997; Roberts et al., 2019; Muxworthy et al., 2023). A subordinate population of non-interacting, SD particles, possibly associated with very fine subdivisions of the submicrometric (<1 μm) lamellae observed in SEM images (Fig. 3), is suggested by the occurrence of narrow ridges along the coercivity (Bu) axis in some FORC diagrams (Fig. 2). Thus, there is likely a minor fraction of ideal magnetic carriers capable of preserving high-fidelity paleointensity records (e.g., Huang et al. 2024). Overall, however, the FORC diagrams exhibit a dominance of distributions with low coercivity and high interaction (e.g., spreading along the interaction field axis), as is typical of PSD/MD grains. We may therefore anticipate that the ZIS dike samples could be complicated by non-ideal magnetic behavior, in which some of Thellier's laws, such as additivity and reciprocity, may not be strictly followed (Néel, 1949; Tauxe et al., 2021). Consequently, our paleointensity estimates are subject to additional uncertainties associated with domain-state effects (MD grains) and magnetic interactions (e.g., Biggin et al., 2007; Dunlop, 2011; Tauxe et al., 2021).

From a paleodirectional perspective, the two sites display distinct magnetization components (Fig. 5). Component A, characterized by low thermal stability, a NNE direction, and steep positive inclinations, is

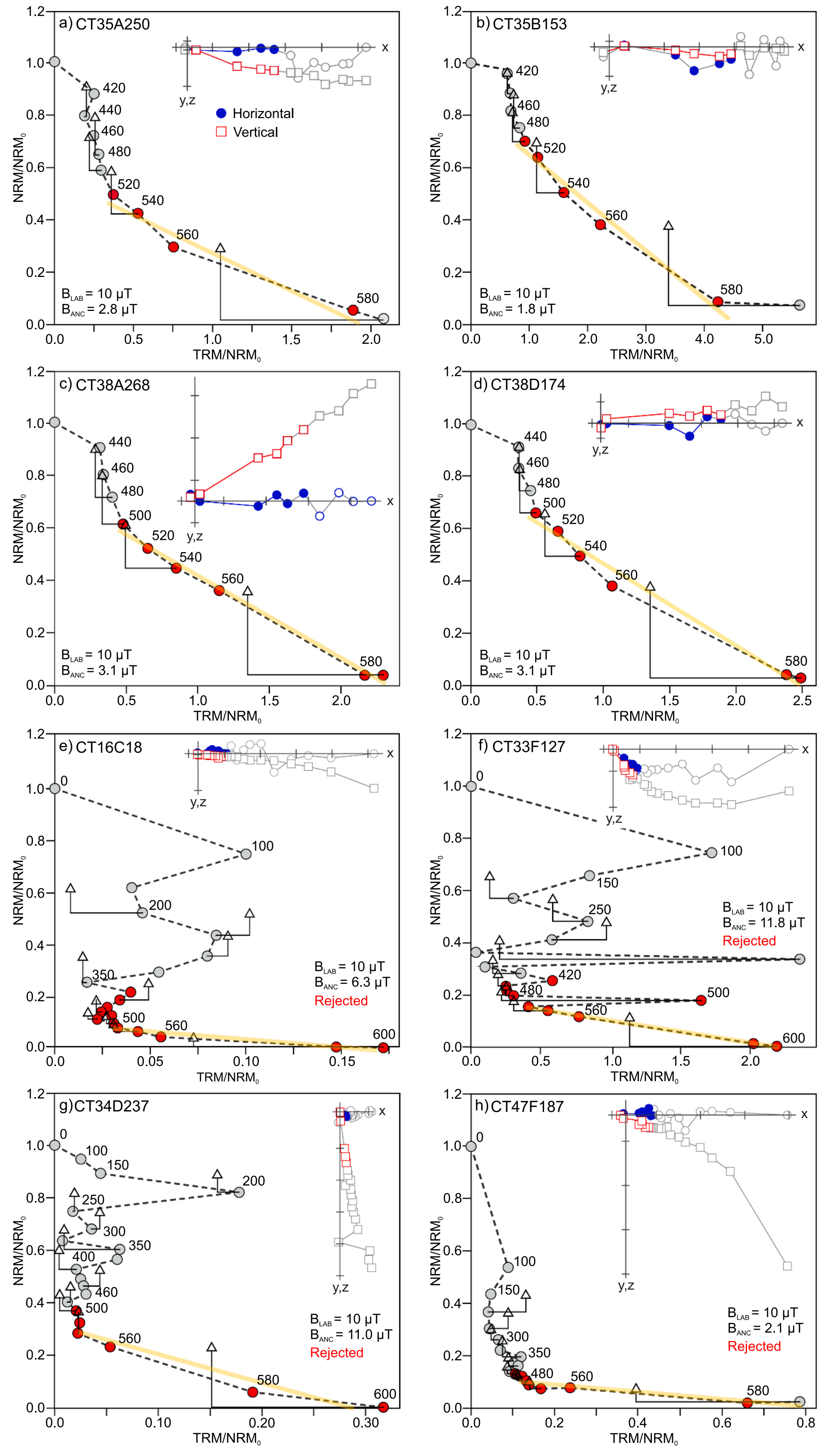

Fig. 6. Representative paleointensity results obtained using the Thellier-Coe protocol. Arai diagrams show the relationship between NRM component remaining and the partial TRM acquired during stepwise thermal demagnetization. Yellow lines highlight the temperature intervals used for paleointensity determinations. Insets show orthogonal projections (Zijderveld plots) with horizontal (blue circles) and vertical (red squares) components. The applied laboratory field (Blab) and the estimated ancient field (Banc) are indicated for each specimen. a-d, h) Specimens that passed the selection criteria and were accepted for paleointensity calculation. e-g) Specimens that failed one or more quality criteria and were rejected.

attributed to pyrrhotite and is directionally similar to a regional Cambro-Ordovician (ca. 480–460 Ma) overprint, possibly related to the post-orogenic thermal collapse of Western Gondwana, as proposed by Bellon et al. (2024) and Gallo et al. (2025). Notably, however, thermochronological data from Hueck et al. (2018a, b) for the Major Gercino Shear Zone do not reflect any regional heating during this interval, but rather a single thermal event in the Early Cretaceous, associated with Paraná LIP magmatism. Alternatively, this magnetization could be linked to the final stages of the Brasiliano Cycle (ca. 570–540 Ma), when subvertical, brittle-ductile NNE-trending structures developed in the region, affecting both the basement granites and the dikes of the ZIS (e.g., Hueck et al., 2018a, b). Component B, defined by NE-SW directions and moderate to shallow inclinations (both positive and negative), isolated between ∼420 °C and 600 °C and associated with titanomagnetite

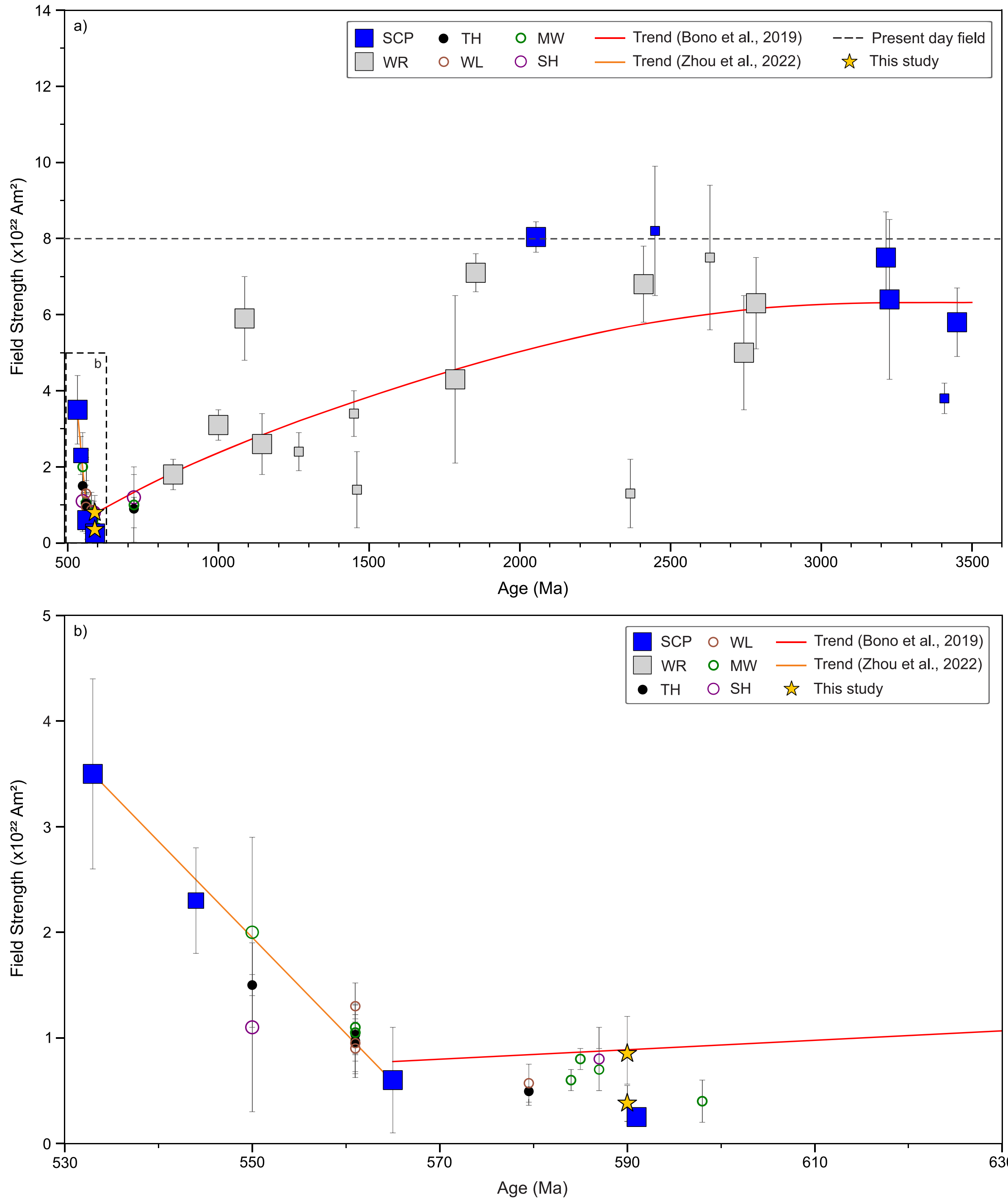

Fig. 7. Field strength through geological time. a) Squares represent paleointensity estimates obtained using thermal Thellier methods: single-crystal (SCP, blue) and whole-rock (WR, gray), updated from Zhou et al. (2024) and Huang et al. (2024). Large squares denote time-averaged paleomagnetic dipole moments (PDM), whereas small squares represent virtual dipole moments (VDM), with reduced symbol size reflecting smaller numbers of determinations relative to Bono et al. (2019) and Zhou et al. (2022). Non-Thellier results are shown as open circles and compiled from Zhou et al. (2022), including microwave (MW, green), Shaw (SH, purple), and Wilson (WL, brown) methods, with symbol sizes scaled by the number of cooling units. Whole-rock Thellier data from the literature are shown as filled black circles (TH) (Thallner et al., 2021a; 2021b and Thallner et al., 2022). Yellow stars mark the VDM values obtained in this study for the two mafic dikes of the Zimbros Intrusive Suite at ca. 590 Ma. The red curve shows the polynomial fit of Bono et al. (2019) for the interval 3450 to 565 Ma and the trend between 565 and 532 Ma proposed by Zhou et al. (2022). The dashed horizontal line indicates the mean strength of the present-day field. Uncertainties are shown as one standard deviation. b) Enlargement of panel (a), highlighting the 530 to 630 Ma interval.

and magnetite, is interpreted as the characteristic remanent magnetization (ChRM). The mean directions calculated for Component B suggest an antipodal relationship between sites CT-35 and CT-38. Despite the limited number of directional records, these directions are in good agreement with coeval mid-Ediacaran (ca. 595–585 Ma) virtual geomagnetic poles from the Río de la Plata Craton (e.g., from the Playa Hermosa, Villa Mónica, and Cerro Largo formations; Rapalini et al., 2013, 2015). This regional consistency supports the interpretation that the directions associated with Component B are primary and record the mid-Ediacaran geomagnetic field. Moreover, the antipodal relationship between the two sites is consistent with a dominantly dipolar field that, according to Bono and Tarduno (2015), may have persisted even under extremely low intensity during the Ediacaran. The relatively high directional dispersion (low k) observed in these data may reflect strong field variability (e.g., Halls et al., 2015), consistent with an otherwise highly unstable geodynamo (e.g., Bono and Tarduno, 2015).

The paleointensity results obtained in this study, although restricted to a limited success rate (~20 %) due to the rigorous exclusion of data exhibiting non-ideal behaviors intrinsic to the lithology, demonstrate internal consistency. Compliance with the QMD quality criterion (Biggin and Paterson, 2014; Bono et al., 2022b) was strictly evaluated through pTRM-tail checks and quantification of Arai plot curvature using the k' parameter (Paterson, 2011). This analysis identified a subset of high-linearity specimens from sites CT-35 and CT-38 that satisfy more restrictive curvature thresholds and yield paleointensity estimates statistically indistinguishable from those obtained using less stringent filters. This stability indicates that the mean intensities are not controlled by marginal data or residual curvature ("sagging"). Although the predominance of MD and PSD grains in the overall dataset (Tauxe et al., 2021) accounts for the high rejection rate, the quality control procedures applied ensure that systematic bias has been removed from the final accepted subset. Even considering persistent methodological limitations, including the absence of explicit anisotropy corrections, the use of a single experimental protocol, and the limited availability of well-defined paleomagnetic directions, the robustness of the results across different filtering levels demonstrates that these data constitute reliable records. In this context, the results presented here meet the requirements for inclusion in global paleointensity compilations, provided they are appropriately filtered and interpreted alongside other Neoproterozoic estimates.

The mean VDM of $0.38 \pm 0.15 \times 10^{22}$ Am^2 (site CT-35) and $0.89 \pm 0.33 \times 10^{22}$ Am^2 (site CT-38), calculated for the two ZIS mafic dikes, support the growing evidence for ultra-low geomagnetic field intensities during the Ediacaran (Fig. 7a). Our results are consistent with other coeval, instantaneous paleointensity estimates (Fig. 7b) reported from Laurentia and Baltica (e.g., Shcherbakova et al., 2020; Thallner et al., 2021a, 2021b; Thallner et al., 2022). Comparable values have also been reported from TAF estimates, such as the Sept-Îles Intrusive Suite (ca. 565 Ma; Bono et al., 2019) and, more recently, the Passo da Fabiana Gabbros (ca. 591 Ma) in the DFB, southern Brazil (Huang et al., 2024), where single-crystal paleointensity (SCP) experiments yielded a PDM of $0.25 \pm 0.02 \times 10^{22}$ Am^2 after anisotropy and cooling-rate corrections (Fig. 7b). Direct comparison within the DFB indicates that the VDM from site CT-35 overlaps with the PDM of the Passo da Fabiana Gabbros within 1σ uncertainty, whereas the CT-38 value is higher. Taken together, these data consistently indicate a weak geomagnetic field at ca. 590 Ma. The agreement between results obtained using different methods, including single-crystal paleointensity (SCP) experiments and whole-rock determinations, and involving magnetic carriers with different domain states, supports the interpretation of a globally extensive, ultra-weak geomagnetic field in the mid-to-late Ediacaran. This interpretation remains valid even when considering the instantaneous nature of the records preserved in the dikes.

The PDM obtained for the Passo da Fabiana Gabbros (ca. 591 Ma; Huang et al., 2024) represents the lowest mean field intensity recorded for the Ediacaran. Together with single-crystal estimates from the Sept-Îles anorthosite (ca. 565 Ma; Bono et al., 2019) and an array of instantaneous paleointensity estimates (e.g., Shcherbakova et al., 2020; Thallner et al., 2021a, 2021b; Thallner et al., 2022; this study), these results indicate a prolonged interval of ultra-low geomagnetic field strength, with intensities ≤10 % of the present-day value, persisting for at least 26 million years. Such weakened and potentially unstable field state, characterized by exceptionally high directional dispersion and a high frequency of reversals (e.g., Bono and Tarduno, 2015; Halls et al., 2015; Bono et al., 2019; Levashova et al., 2021), is consistent with geodynamo models predicting a low-efficiency dynamo regime preceding inner core nucleation (e.g., Driscoll, 2016; Davies et al., 2022). According to these models, inner core nucleation likely occurred around 550 Ma (Zhou et al., 2022, 2024).

6. Conclusions

This study presents new directional and absolute paleointensity data obtained from two mafic dikes of the Zimbros Intrusive Suite (ca. 590 Ma) in southern Brazil. Despite the inherent limitation of the instantaneous nature of the records, these results provide a valuable contribution to the Ediacaran paleomagnetic database, offering insights into the instantaneous behavior of the geomagnetic field outside the Laurentia and Baltica paleocontinents. Directional analyses reveal two distinct magnetization components. The high-temperature component, interpreted as the ChRM, is consistent with a predominantly dipolar (GAD) field, as indicated by the antipodal relationship between the sites, which persisted even under ultra-low field conditions.

Absolute paleointensity experiments conducted using the Thellier-Coe protocol yielded VDM estimates of $0.38 \pm 0.15 \times 10^{22}$ Am^2 and $0.89 \pm 0.33 \times 10^{22}$ Am^2. Although the dataset is dominated by non-ideal (PSD-MD) magnetic grains, the mean estimates remain stable under progressively restrictive quality criteria, even with a reduction in the number of accepted specimens, indicating that the obtained values are not dominated by effects associated with Arai curvature. These results are consistent with coeval estimates from Laurentia and Baltica and show remarkable regional agreement with the PDM determined from the Passo da Fabiana Gabbros. This consistency, observed across distinct methods (whole rock vs. SCP) and different magnetic domain states (PSD/MD vs. SD), corroborates the interpretation of a genuine ultra-weak geomagnetic field state in the mid-to-late Ediacaran.

These new data support the idea of a prolonged ultra-low geomagnetic field interval of at least 26 million years, as previously claimed by Huang et al. (2024). This field state is compatible with thermodynamic and geodynamical predictions associated with a low-efficiency geodynamo regime immediately prior to the onset of inner core nucleation.

Future investigations should include new determinations of paleointensity, both spot and time-averaged, in coeval Gondwana units. Expanding such records will be essential to further constrain the duration, intensity, and global extent of this anomalous geomagnetic field regime during the Ediacaran.

CRediT authorship contribution statement

Camila R. Tomé: Writing – review & editing, Writing – original draft, Visualization, Validation, Supervision, Methodology, Investigation, Formal analysis, Data curation, Conceptualization. **Jairo F. Savian:** Writing – review & editing, Writing – original draft, Visualization, Validation, Supervision, Project administration, Investigation, Funding acquisition, Conceptualization. **Wellington P. de Oliveira:** Writing – review & editing, Writing – original draft, Methodology, Investigation, Formal analysis, Conceptualization. **Gelvam A. Hartmann:** Writing – review & editing, Validation, Supervision, Methodology, Conceptualization. **João A.S. Fontoura:** Methodology, Investigation, Data curation, Conceptualization. **Mathew Domeier:** Writing – review & editing, Supervision, Methodology, Investigation, Data curation, Conceptualization. **Filipe A. Temporim:** Validation, Investigation, Data curation. **Ruth Hinrichs:** Methodology, Formal analysis, Data curation. **Ricardo I.F. Trindade:** Validation, Data curation. **Maria de Fátima Bitencourt:** Writing – review & editing, Writing – original draft, Validation, Supervision, Project administration, Funding acquisition, Conceptualization.

Declaration of competing interest

The authors declare that they have no known competing financial interests or personal relationships that could have appeared to influence the work reported in this paper.

Acknowledgements

This study was financed by the Brazilian National Council for Scientific and Technological Development (CNPq) through Productivity Grant process 311486/2015–0 to M.F. Bitencourt and a PhD scholarship to C.R. Tomé (grant 152082/2021–2). Financial support by the Rio Grande do Sul State Research Foundation (FAPERGS, project 24/2551-0001541-8) awarded to J.F. Savian is also acknowledged, as well as logistic support from Programa de Pós-graduação em Geociências / UFRGS during fieldwork. W.P. de Oliveira acknowledges support from the São Paulo Research Foundation (FAPESP, grant #2023/13612–6). G.A. Hartmann acknowledges support from CNPq (grant 305110/2023–3) and São Paulo Research Foundation (FAPESP, grant #2023/04179–7). J.F. Savian also acknowledges support from CNPq (grants 304022/2018–7 and 311231/2021–7). M. Domeier acknowledges support by the European Research Council (ERC) under the European Union's Horizon 2020 research and innovation programme (grant agreement No. 101043844) and from the Research Council of Norway through its Centres of Excellence funding scheme, project 332523 (Centre for Planetary Habitability). Part of this work was conducted at the USPMag Laboratory, Institute of Astronomy, Geophysics and Atmospheric Sciences (IAG), University of São Paulo (USP), with funding from CAPES, FAPESP, and CNPq. We thank the two anonymous reviewers for their thoughtful evaluations of the manuscript and appreciate the careful editorial handling by Carolina Lithgow-Bertelloni.

Supplementary materials

Supplementary material associated with this article can be found, in the online version, at doi:10.1016/j.epsl.2026.119961.

Data availability

The raw paleointensity datasets supporting this study are available in the Zenodo repository at https://doi.org/10.5281/zenodo.18926662.

References

Abrajevitch, A., Van der Voo, R., 2010. Incompatible ediacaran paleomagnetic directions suggest an equatorial geomagnetic dipole hypothesis. Earth Planet. Sci. Lett. 293, 164–170. https://doi.org/10.1016/j.epsl.2010.02.038.

Bazhenov, M.L., Levashova, N.M., Meert, J.G., Golovanova, I.V., Danukalov, K.N., Fedorova, N.M., 2016. Late ediacaran magnetostratigraphy of Baltica: evidence for magnetic field hyperactivity? Earth Planet. Sci. Lett. 435, 124–135. https://doi.org/10.1016/j.epsl.2015.12.015.

Bellon, U.D., Trindade, R.I.F., Williams, W., Galante, D., Sant'Anna, L.G., Pescarini, T., 2024. Clay minerals and continental-scale remagnetization: a case study of South American neoproterozoic carbonates. J. Geophys. Res. 129 (10). https://doi.org/10.1029/2023JB028538.

Béguin, A., Paterson, G.A., Biggin, A.J., de Groot, L.V., 2020. Paleointensity.Org: an online, open source, application for the interpretation of paleointensity data. Geochem. Geophys. Geosyst. 21, e2019GC008791.

Biggin, A.J., Perrin, M., Dekkers, M.J., 2007. A reliable absolute palaeointensity determination obtained from a non-ideal recorder. Earth Planet. Sci. Lett. 257, 545–563. https://doi.org/10.1016/j.epsl.2007.03.017.

Biggin, A.J., Paterson, G.A., 2014. A new set of qualitative reliability criteria to aid inferences on paleomagnetic dipole moment variations through geological time. Front. Earth Sci. 2, 24. https://doi.org/10.3389/feart.2014.00024.

Bitencourt, M.F., Nardi, L.V.S., 2000. Tectonic setting and sources of magmatism related to the Southern Brazilian Shear Belt. Rev. Bras. Geociênc. 30 (1), 186–189.

Bitencourt, M.F., Hackspacher, P.C., Nardi, L.V.S., 1989a. A Zona de Cisalhamento Major Gercino - Santa Catarina. Simpósio Nacional de Estudos Tectônicos 1989, 214–216.

Bitencourt, M.F., 1996. Granitóides sintectônicos da região de Porto Belo, SC: uma abordagem petrológica e estrutural do magmatismo em zonas de cisalhamento. [Tese] Instituto de Geociências. Universidade Federal do Rio Grande do Sul, p. 310. http://hdl.handle.net/10183/225804.

Bono, R.K., Tarduno, J.A., 2015. A stable ediacaran Earth recorded by single silicate crystals of the ca. 565 ma Sept-Îles intrusion. Geology 43, 131–134. https://doi.org/10.1130/G36247.1.

Bono, R.K., Tarduno, J.A., Nimmo, F., Cottrell, R.D., 2019. Young inner core inferred from Ediacaran ultra-low geomagnetic field intensity. Nat. Geosci. 12, 143–147. https://doi.org/10.1038/s41561-018-0288-0.

Bono, R.K., et al., 2022a. The PINT database: a definitive compilation of absolute paleomagnetic intensity determinations since 4 billion years ago. Geophys. J. Int. 229, ggab490.

Bono, R.K., Paterson, G.A., Biggin, A.J., 2022b. MCADAM: a continuous paleomagnetic dipole moment model for at least 3.7 billion years. Geophys. Res. Lett. 49, e2022GL100898.

Chemale Jr, F., Mallmann, G., Bitencourt, M.F., Kawashita, K., 2012. Time constraints on magmatism along the Major Gercino Shear Zone, southern Brazil: implications for West Gondwana reconstruction. Gondwana Res 22, 184–199. https://doi.org/10.1016/j.gr.2011.08.018.

Coe, R.S., 1967. Paleo-intensities of the Earth's magnetic field determined from tertiary and quaternary rocks. J. Geophys. Res. 72, 3247–3262. https://doi.org/10.1029/JZ072i012p03247.

Cottrell, R.D., Bono, R.K., Channell, J.E.T., Bunge, H.-P., Tarduno, J.A., 2023. No late cretaceous true polar wander oscillation and implications for stability of Earth relative to the rotation axis. Earth Planet. Sci. Lett. 620, 118338. https://doi.org/10.1016/j.epsl.2023.118338.

Davies, C.J., Bono, R.K., Meduri, D.G., Aubert, J., Greenwood, S., Biggin, A.J., 2022. Dynamo constraints on the long-term evolution of Earth's magnetic field strength. Geophys. J. Int. 228, 316–336. https://doi.org/10.1093/gji/ggab342.

Day, R., Fuller, M., Schmidt, V.A., 1977. Hysteresis properties of titanomagnetites: grain-size and compositional dependence. Phys. Earth Planet. Inter. 13, 260–267. https://doi.org/10.1016/0031-9201(77)90108-X.

De Toni, G.B., Bitencourt, M.F., Nardi, L.V.S., Florisbal, L.M., Almeida, B.S., Geraldes, M., 2020. Dom Feliciano Belt orogenic cycle tracked by its pre-collisional magmatism: the Tonian (ca. 800 Ma) Porto Belo Complex and its correlations in southern Brazil and Uruguay. Precambrian Res 342, 105702. https://doi.org/10.1016/j.precamres.2020.105702.

De Toni, G.B., Bitencourt, M.F., Florisbal, L.M., Martini, A., Nardi, L.V.S., 2024. Anatomy of the transpressional Dom Feliciano Belt and its pre-collisional isotopic (Sr-Nd) signatures: a contribution towards an integrated model for the Brasiliano/Pan-African orogenic cycle. Gondwana Res 125, 180–209. https://doi.org/10.1016/j.gr.2023.08.008.

Domeier, M., Robert, B., Meert, J.G., Kulakov, E.V., McCausland, P.J., Trindade, R.I.F., Torsvik, T.H., 2023. The enduring Ediacaran paleomagnetic enigma. Earth Sci. Rev. 242. https://doi.org/10.1016/j.earscirev.2023.104444.

Dominguez, A.R., Van der Voo, R., Torsvik, T.H., Hendriks, B.W., Abrajevitch, A., Domeier, M., Rousse, S., 2011. The 270 ma palaeolatitude of Baltica and its significance for Pangea models. Geophys. J. Int. 186, 529–550. https://doi.org/10.1111/j.1365-246X.2011.05061.x.

Driscoll, P.E., 2016. Simulating 2Ga of geodynamo history. Geophys. Res. Lett. 43, 5680–5687. https://doi.org/10.1002/2016GL068858.

Dunlop, D.J., Özdemir, O., 1997. Rock Magnetism: Fundamentals and Frontiers. Cambridge University Press, United Kingdom, p. 573.

Dunlop, D.J., 2002. Theory and application of the day plot (Mrs/Ms versus Hcr/Hc) 1: theoretical curves and tests using titanomagnetite data. J. Geophys. Res. 107, 2056. https://doi.org/10.1029/2001JB000486.

Dunlop, D.J., 2011. Physical basis of the Thellier-Thellier and related paleointensity methods. Phys. Earth Planet. Inter. 187, 118–138.

Fisher, R., 1953. Dispersion on a sphere. Proc. R. Soc. Lond. A 217, 295–305. https://doi.org/10.1098/rspa.1953.0064.

Gallo, L.C., Domeier, M., Antonio, P.Y., Sapienza, F., Rapalini, A., Font, E., Warren, L., 2025. Unraveling remagnetization sources using statistical learning. Earth Planet. Sci. Lett. 662. https://doi.org/10.1016/j.epsl.2025.119390.

Haggerty, S.E., 1991. Oxide textures – a mini-atlas. In: Lindsley, D.H. (Ed.), Oxide Minerals: Petrologic and Magnetic Significance. De Gruyter, pp. 129–220. https://doi.org/10.1515/9781501508684-008.

Halls, H.C., Lovette, A., Hamilton, M., Söderlund, U., 2015. A paleomagnetic and U-Pb geochronology study of the western end of the Grenville dyke swarm: rapid changes in paleomagnetic field direction at ca. 585 ma related to polarity reversals? Precambrian Res 257, 137–166. https://doi.org/10.1016/j.precamres.2014.11.029.

Harrison, R.J., Feinberg, J.M., 2008. FORCinel: an improved algorithm for calculating first-order reversal curve distributions using locally weighted regression smoothing. Geochem. Geophys. Geosyst. 9, Q05016. https://doi.org/10.1029/2008GC001987.

Huang, W., Tarduno, J.A., Zhou, T., Ibañez-Mejia, M., Dal Olmo-Barbosa, L., Koester, E., 2024. Near-collapse of the geomagnetic field may have contributed to atmospheric oxygenation and animal radiation in the ediacaran Period. Commun. Earth Environ. 5, 207. https://doi.org/10.1038/s43247-024-01360-4.

Hueck, M., Basei, M.A.S., Wemmer, K., Oriolo, S., Heidelbach, F., Siegesmund, S., 2018a. Evolution of the major Gercino shear zone in the Dom Feliciano Belt, south Brazil, and implications for the assembly of southwestern Gondwana. Int. J. Earth Sci. 108 (2), 403–425. https://doi.org/10.1007/s00531-018-1660-4.

Hueck, M., Dunkl, I., Heller, B., Stipp Basei, M.A., Siegesmund, S., 2018b. U-Th)/He thermochronology and zircon radiation damage in the South American passive margin: thermal overprint of the Paraná LIP? Tectonics 37 (10), 4068–4085. https://doi.org/10.1029/2018TC005041.

Kirschvink, J.L., 1980. The least-squares line and plane and the analysis of palaeomagnetic data. Geophys. J. R. Astron. Soc. 62, 699–718. https://doi.org/10.1111/j.1365-246X.1980.tb02601.x.

Levashova, N.M., Golovanova, I.V., Rudko, D.V., Danukalov, K.N., Rudko, S.V., Yu, S.R., Meert, J.G., 2021. Late ediacaran magnetic field hyperactivity: quantifying the reversal frequency in the Zigan Formation. Southern Urals, Russia. Gondwana Res. 94, 133–142. https://doi.org/10.1016/j.gr.2021.02.018.

Li, Z.X., Evans, D.A., Halverson, G.P., 2013. Neoproterozoic glaciations in a revised global palaeogeography from the breakup of Rodinia to the assembly of

Gondwanaland. Sediment. Geol. 294, 219–232. https://doi.org/10.1016/j.sedgeo.2013.05.016.
Maxbauer, D.P., Feinberg, J.M., Fox, D.L., 2016. MAX UnMix: a web application for unmixing magnetic coercivity distributions. Comput. Geosci. 95, 140–145. https://doi.org/10.1016/j.cageo.2016.07.009.
Meert, J.G., Levashova, N.M., Bazhenov, M.L., Landing, E., 2016. Rapid changes of magnetic field polarity in the late Ediacaran: linking the Cambrian evolutionary radiation and increased UV-B radiation. Gondwana Res 34, 149–157. https://doi.org/10.1016/j.gr.2016.01.001.
Meert, J.G., Van der Voo, R., Powell, C.M., Li, Z.X., McElhinny, M.W., Chen, Z., Symons, D.T.A., 1993. A plate-tectonic speed limit? Nature 363, 216–217. https://doi.org/10.1038/363216a0.
Muxworthy, A.R., Turney, J.N., Qi, L., Baker, E.B., Perkins, J.R., Abdulkarim, M.A., 2023. Interpreting high-temperature magnetic susceptibility data of natural systems. Front. Earth Sci. 11, 1171200. https://doi.org/10.3389/feart.2023.1171200.
Nagata, T., Arai, Y., Momose, K., 1963. Secular variation of the geomagnetic total force during the last 5000 years. J. Geophys. Res. 68, 5277–5281. https://doi.org/10.1029/j.2156-2202.1963.tb00005.x.
Néel, L., 1949. Théorie du traînage magnétique des ferromagnétiques en grains fins avec applications aux terres cuites. Ann. Géophys. 5, 99–136.
Och, L.M., Shields-Zhou, G.A., 2012. The neoproterozoic oxygenation event: environmental perturbations and biogeochemical cycling. Earth Sci. Rev. 110, 26–57. https://doi.org/10.1016/j.earscirev.2011.09.004.
Oriolo, S., Oyhantçabal, P., Wemmer, K., Siegesmund, S., 2017. Contemporaneous assembly of Western Gondwana and final Rodinia breakup: implications for the supercontinent cycle. Geosci. Front. 8, 1431–1445. https://doi.org/10.1016/j.gsf.2017.01.009.
Paterson, G.A., 2011. A simple test for the presence of multidomain behavior during paleointensity experiments. J. Geophys. Res. 116, B10104. https://doi.org/10.1029/2011JB008369.
Paterson, G.A., Tauxe, L., Biggin, A.J., Shaar, R., Jonestrask, L.C., 2014. On improving the selection of Thellier-type paleointensity data. Geochem. Geophys. Geosyst. 15, 1180–1192. https://doi.org/10.1002/2013GC005135.
Paterson, G.A., Biggin, A.J., Hodgson, E., Hill, M.J., 2015. Thellier-type paleointensity data from multidomain specimens. Phys. Earth Planet. Inter. 245, 117–133. https://doi.org/10.1016/j.pepi.2015.06.003.
Peruchi, F.M., Florisbal, L.M., Bitencourt, M.F., Padilha, D.F., Nardi, L.V.S., 2021. Ediacaran post-collisional K-rich granitic magmatism within the Major Gercino Shear Zone, southern Brazil: an example of prolonged magmatism and differentiation under active transcurrent tectonism. Lithos 402, 106341. https://doi.org/10.1016/j.lithos.2021.106341.
Rapalini, A.E., Trindade, R.I.F., Poiré, D.G., 2013. The La Tinta pole revisited: paleomagnetism of the neoproterozoic Sierras Bayas Group (Argentina) and its implications for Gondwana and Rodinia. Precambr. Res. 224, 51–70. https://doi.org/10.1016/j.precamres.2012.09.007.
Rapalini, A.E., Tohver, E., Bettucci, L.S., Lossada, A.C., Barcelona, H., Pérez, C., 2015. The late neoproterozoic Sierra de las Ánimas Magmatic Complex and Playa Hermosa Formation, southern Uruguay, revisited: paleogeographic implications of new paleomagnetic and precise geochronologic data. Precambr. Res. 259, 143–155. https://doi.org/10.1016/j.precamres.2014.11.021.
Robert, B., Domeier, M., Jakob, J., 2021. On the origins of the Iapetus ocean. Earth-Sci. Rev. 221, 103791. https://doi.org/10.1016/j.earscirev.2021.103791.
Robert, B., Corfu, F., Domeier, M., Blein, O., 2023. Evidence for large disturbances of the Ediacaran geomagnetic field from West Africa. Precambrian Res 394, 107095. https://doi.org/10.1016/j.precamres.2023.107095.
Roberts, A.P., Pike, C.R., Verosub, K.L., 2000. First-order reversal curve diagrams: a new tool for characterizing the magnetic properties of natural samples. J. Geophys. Res. Solid Earth 105, 28461–28475. https://doi.org/10.1029/2000jb900326.
Roberts, A.P., Hu, P.X., Harrison, R.J., Heslop, D., Muxworthy, A.R., Oda, H., Sato, T., Tauxe, L., Zhao, X., 2019. Domain state diagnosis in rock magnetism: evaluation of potential alternatives to the Day diagram. J. Geophys. Res. Solid Earth 124, 5286–5314. https://doi.org/10.1029/2018JB017049.
Rochette, P., Fillion, G., Mattéi, J.L., Dekkers, M.J., 1990. Magnetic transition at 30–34 kelvin in pyrrhotite: insight into a widespread occurrence of this mineral in rocks. Earth Planet. Sci. Lett. 98, 319–328. https://doi.org/10.1016/0012-821X(90)90034-U.
Shaar, R., Tauxe, L., 2015. Instability of thermoremanence and the problem of estimating the ancient geomagnetic field strength from non-single-domain recorders. Proc. Natl. Acad. Sci. U.S.A. 112, 11187–11192. https://doi.org/10.1073/pnas.1507986112.
Shcherbakova, V.V., Bakhmutov, V.G., Thallner, D., Shcherbakov, V.P., Zhidkov, G.V., Biggin, A.J., 2020. Ultra-low palaeointensities from East European Craton, Ukraine support a globally anomalous palaeomagnetic field in the Ediacaran. Geophys. J. Int. 220, 1920–1946. https://doi.org/10.1093/gji/ggz566.
Tarduno, J.A., Zhou, T., Huang, W., Jodder, J., 2025. Earth's magnetic field and its relationship to the origin of life, evolution and planetary habitability. Natl. Sci. Rev. 12, nwaf082. https://doi.org/10.1093/nsr/nwaf082.
Tauxe, L., Shaar, R., Jonestrask, L., Swanson-Hysell, N.L., Minnett, R., Koppers, A.A.P., Fairchild, L., et al., 2016. PmagPy: software package for paleomagnetic data analysis and a bridge to the Magnetics Information Consortium (MagIC) Database. Geochem. Geophys. Geosyst. 17, 2450–2463. https://doi.org/10.1002/2016GC006307.
Tauxe, L., Santos, C.N., Cych, B., Zhao, X., Roberts, A.P., Nagy, L., Williams, W., 2021. Understanding non-ideal paleointensity recording in igneous rocks: insights from aging experiments on Lava Samples and the causes and Consequences of "fragile. Curvature in Arai Plots. Geochem. Geophys. Geosyst. 22, e2020GC009423.
Thallner, D., Biggin, A.J., Halls, H.C., 2021a. An extended period of extremely weak geomagnetic field suggested by palaeointensities from the Ediacaran Grenville DIKES (SE Canada). Earth Planet. Sci. Lett. 568, 117025. https://doi.org/10.1016/j.epsl.2021.117025.
Thallner, D., Biggin, A.J., McCausland, P.J.A., Fu, R.R., 2021b. New paleointensities from the Skinner Cove Formation, Newfoundland, suggest a changing state of the geomagnetic field at the ediacaran-cambrian transition. J. Geophys. Res. Solid Earth 126. https://doi.org/10.1029/2021JB022292.
Thallner, D., Shcherbakova, V.V., Bakhmutov, V.G., Shcherbakov, V.P., Zhidkov, G.V., Poliachenko, I.B., Biggin, A.J., 2022. New palaeodirections and palaeointensity data from extensive profiles through the Ediacaran section of the Volyn Basalt Province (NW Ukraine). Geophys. J. Int. 231, 474–492. https://doi.org/10.1093/gji/ggac186.
Thellier, E., Thellier, O., 1959. Sur l'intensité du champ magnétique terrestre dans le passé historique et géologique. Ann. Géophys. 15, 285–376.
Tomé, C.R., Bitencourt, M.F., Raposo, M.I.B., Savian, J.F., 2020. Magnetic fabric data on interactive syntectonic magmas of contrasting composition in composite dikes from south Brazil. J. Geodyn. 138, 101754. https://doi.org/10.1016/j.jog.2020.101754.
Wen, B., Luo, C., Li, Y.X., Lin, Y., 2022. Late ediacaran inertial-interchange true polar wander (IITPW) event: a new road to reconcile the enigmatic paleogeography prior to the final assembly of Gondwana. Turk. J. Earth Sci. 31 (5), 425–437. https://doi.org/10.55730/1300-0985.1811.
Xiao, S.H., Narbonne, G.M., 2020. The Ediacaran period. In: Gradstein, F.M., Ogg, J.G., Schmitz, M.D., Ogg, G.M. (Eds.), Geologic Time Scale 2020. Elsevier, pp. 521–561.
Zahirovic, S., Müller, R.D., Seton, M., Flament, N., 2015. Tectonic speed limits from plate kinematic reconstructions. Earth Planet. Sci. Lett. 418, 40–52. https://doi.org/10.1016/j.epsl.2015.02.037.
Zhou, T., Tarduno, J.A., Nimmo, F., Cottrell, R.D., Bono, R.K., Ibañez-Mejía, M., Huang, W., Hamilton, M., Kodama, K.P., Smirnov, A.V., Crummins, B., Padgett, F., 2022. Early cambrian renewal of the geodynamo and the origin of inner core structure. Nat. Commun. 13, 4161. https://doi.org/10.1038/s41467-022-31677-7.
Zhou, T., Ibañez-Mejia, M., Bono, R.K., Cottrell, R.D., Bleeker, W., Kodama, K.P., Smirnov, A.V., Crummins, B., Padgett, F., Tarduno, J.A., 2024. Magnetization and age of ca. 544 ma syenite, eastern Canada: evidence for renewal of the geodynamo. Earth Planet. Sci. Lett. 639, 118758. https://doi.org/10.1016/j.epsl.2024.118758.